LETTER

Ptychographic X–ray computed tomography at the nanoscale

Martin Dierolf[1], Andreas Menzel[2], Pierre Thibault[1], Philipp Schneider[3], Cameron M. Kewish[2]†, Roger Wepf[4], Oliver Bunk[2] & Franz Pfeiffer[1]

X-ray tomography is an invaluable tool in biomedical imaging. It can deliver the three-dimensional internal structure of entire organisms as well as that of single cells, and even gives access to quantitative information, crucially important both for medical applications and for basic research[1–4]. Most frequently such information is based on X-ray attenuation. Phase contrast is sometimes used for improved visibility but remains significantly harder to quantify[5,6]. Here we describe an X-ray computed tomography technique that generates quantitative high-contrast three-dimensional electron density maps from phase contrast information without reverting to assumptions of a weak phase object or negligible absorption. This method uses a ptychographic coherent imaging approach to record tomographic data sets, exploiting both the high penetration power of hard X-rays and the high sensitivity of lensless imaging[7–9]. As an example, we present images of a bone sample in which structures on the 100 nm length scale such as the osteocyte lacunae and the interconnective canalicular network are clearly resolved. The recovered electron density map provides a contrast high enough to estimate nanoscale bone density variations of less than one per cent. We expect this high-resolution tomography technique to provide invaluable information for both the life and materials sciences.

The high penetration power of X-rays provides the ability to see inside macroscopic objects in a non-invasive way. Computed tomography instruments are used for medical applications, which typically produce three-dimensional (3D) attenuation maps with a spatial resolution of just below a cubic millimetre. Other dedicated high-resolution micro-tomography techniques at brilliant synchrotron sources allow 3D imaging of biological and materials science samples at resolutions better than 100 nm (refs 1–4). So far, these high-resolution methods have been used mostly for morphological analysis, where it is sufficient to image a specimen with coarsely resolved 'grey levels' that are not necessarily related to a significant physical quantity. However, there is a growing number of applications which require both quantitative and sensitive investigation methods. Among such applications is the study of osteoporosis, the most prevalent degenerative disease in western society. Diagnosis of osteoporosis and monitoring of the effectiveness of its treatment requires quantitative assessment of both the morphological and density changes in the bone tissue.

The downside of the high penetration power of X-rays is their low absorption contrast. In fact, absorption tends to decrease with the fourth power of photon energy whereas phase contrast scales with the inverse square of the energy. Thus, in the case of ångstrom-wavelength radiation, most materials exhibit phase changes that are more pronounced by orders of magnitude than their respective absorption variations. However, as in the optical regime, X-ray phase shifts are significantly more challenging to detect and to quantify. Various schemes have been implemented[5,6,10–13] and are in frequent use for contrast enhancement both in two and in three dimensions. Yet quantitative analysis often is limited in resolution or depends on simplifying assumptions, such as the absence of absorption or the restriction to small phase shifts only, which are frequently violated in the case of extended 3D samples.

Significantly less stringent are the analytical requirements for coherent diffractive imaging (CDI) to provide quantitative phase information with high resolution and high sensitivity. CDI is based on the retrieval of image information from precise measurements in the far field of coherent light scattered by the specimen[7]. By doing away with the optics, CDI techniques offer—in principle—optimal sensitivity for a given radiation dose. Among recent developments, a scanning method called ptychographic CDI was shown to be especially robust and reliable[14–16] and can now be performed routinely at several instruments worldwide[9,17–20]. Because the reconstructed quantity is the complex-valued wave field past the specimen, the method is inherently quantitative. The reconstruction does not rely on assumptions of homogeneity, negligible absorption, or small phase advance.

Here we report the first implementation of ptychographic X-ray computed tomography, which exploits the high phase sensitivity of two-dimensional (2D) coherent diffractive imaging to generate quantitative 3D density maps of extended specimens on the nanoscale. The experimental set-up, shown in Fig. 1, is reminiscent of first-generation computed tomography, in which a pencil X-ray beam was scanned over the sample and a point detector following the motion of the source measured the beam attenuation. This procedure was repeated for a complete range of 180 degrees in sample orientation. Similarly, in our nano-tomography experiment, a coherent portion of a monochromatized incoming X-ray beam is selected with a pinhole of diameter about 2.3 μm. But unlike first-generation computed tomography, the detector in our experiment collects not only the transmitted beam intensity, but its full diffracted intensity distribution downstream of the specimen. The coherence of the incoming beam allows the reconstruction of the wave field distribution for each projection at a resolution much higher than the spot size on the specimen. These high-resolution 2D projections are then further processed using computed tomography algorithms to reconstruct the sample's 3D refractive index distribution.

As a demonstration of the capabilities of the new technique and its potential value, particularly for biomedical research applications, we present the study of a cortical bone specimen taken from the mid-diaphysis of a mouse femur. Bones exhibit a hierarchy of multi-scale structural characteristics, which are associated with their fundamental biomechanical properties and their eventual degradation due to diseases. The associated length scales cover a wide range, from centimetres down to nanometres, and at the smallest scales bone samples remain difficult to image because they are composed of a highly structured mesh of mineral and organic elements.

Unlike in traditional X-ray microscopy, the recovered images are complex-valued maps that encode both the absorption and the

---

[1]Department of Physics (E17), Technische Universität München, 85748 Garching, Germany. [2]Swiss Light Source, Paul Scherrer Institut, 5232 Villigen PSI, Switzerland. [3]Institute for Biomechanics, ETH Zurich, 8093 Zurich, Switzerland. [4]Electron Microscopy ETH Zurich (EMEZ), 8093 Zurich, Switzerland. † Present address: Synchrotron SOLEIL, Saint-Aubin BP-48, 91192 Gif-sur-Yvette, France.
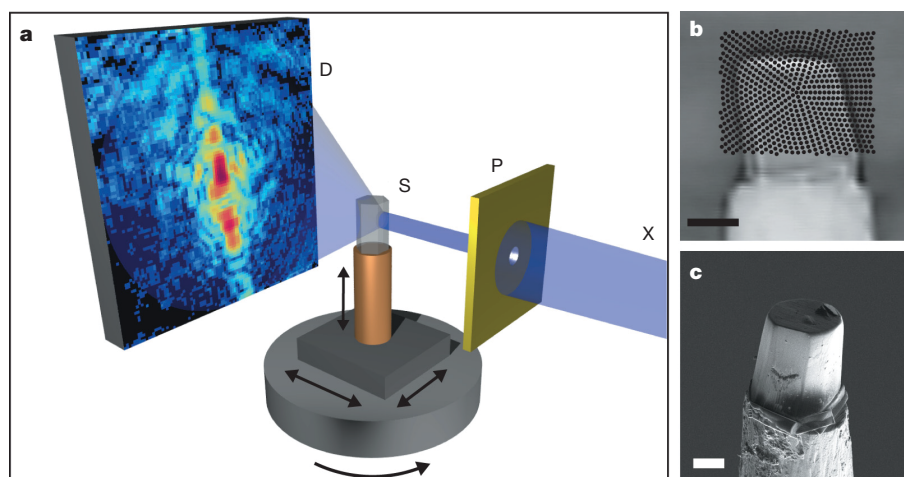
Figure 1 | Experimental set-up and sample.
a, Schematic of experimental set-up. The X-ray beam (X) impinges on the pinhole (P), which creates a localized illumination on the sample (S). Diffraction patterns are recorded with a two-dimensional pixellated detector D. One out of the 704 diffraction patterns per projection is shown. **b**, Projection image of the bone specimen as seen on a scintillator screen imaged with a video microscope used for alignment purposes. The scan points indicated by the black dots cover a rectangular area of 40 μm × 32 μm and are placed on concentric circles starting from the centre. **c**, Scanning electron micrograph of the specimen. Scale bars, 10 μm.

phase shift produced by the sample. The reconstructed transmission function is well modelled by the projection approximation:

$$T(x,y) = \exp\left(\frac{2\pi i}{\lambda} \int \delta(r) + i\beta(r)\mathrm{d}z\right)$$

where λ is the wavelength, $n = 1 - \delta - i\beta$ is the complex-valued space-dependent refractive index, and the integral is taken along the propagation direction. Absorption-based imaging, sensitive only to β in this equation, is characterized by an exponential decay of the signal with the sample thickness, thus confining it to the interval $0 < |T| \leq 1$. In contrast, the complex-valued transmission function can take any value in the unit disk of the complex plane, as though curling the signal around the origin (see Supplementary Fig. 1). The important consequence is that phase shift sensitivity does not decrease as a function of the sample thickness. Still, thicker samples can shift the phase by more than 2π, a phenomenon called phase wrapping. This causes discontinuities when mapping the measurable quantity T to a phase, which is limited to an interval spanning 2π. Using spatial correlations in the image, various methods allow the phase to be reliably unwrapped. In addition to the intrinsically weaker absorption contrast, the transmission function amplitude is observed to be much more affected by intensity variations in the incident beam than the phase part, a property also noted for other phase-contrast imaging modalities[21]. The resulting difference in signal-to-noise ratio is apparent in the line profiles of Fig. 2.

Using ptychographic reconstruction combined with an automated unwrapping procedure for the initially reconstructed phase-contrast projections (see Methods), high-resolution projection images were obtained for sample orientations ranging from −90 to 90 degrees, spaced at one degree intervals (see Supplementary Movie 1). This procedure was followed by a filtered back-projection computed

tomography reconstruction. The result is a 3D map of the real part of the refractive index δ, the spatial variations of which provide direct morphometric information on the sample. A volume rendering of the reconstructed 3D density of the bone sample is shown in Fig. 3 (see also Supplementary Movie 3). Clearly resolved are an osteocyte lacuna (a cavity in the bone matrix in which an osteocyte resides) and the complex network of channels called canaliculi, which extend in all directions over a distance of several micrometres. The lacuno-canalicular network is the subject of intensive investigations because it is known to play a central role in bone modelling and remodelling processes[22]. Morphological analysis of the lacuno-canalicular network can be achieved with other types of measurements[23]. Confocal laser scanning microscopy is widely available but requires multiple steps for sample preparation, including decalcification and labelling, for example, by silver stains or fluorescent markers. Alternatively, electron microscopy can reach nanometre resolutions, but true 3D information is gained only through sectioning. In contrast, X-rays offer the unparalleled benefit of allowing most samples to remain nearly in their native state.

For X-ray energies far from the absorption edges of the atomic species composing the object, the refractive index of a compound material is, to a very good approximation, directly proportional to its electron density distribution. This fact allows a completely quantitative interpretation of the reconstructed density. Figure 4a and b show two slices from the recovered density, with the grey level indicating the local electron density in units of electrons per cubic ångstrom, averaged over one reconstruction voxel of dimensions $(65\ \mathrm{nm})^3$. This quantity is an absolute value: the proportionality between the unitless refractive index and the electron density involves only fundamental constants, and no important source of error impedes the accurate setting of the origin of the density scale. The histogram of all density values is presented in Fig. 4c. The average bone electron density is
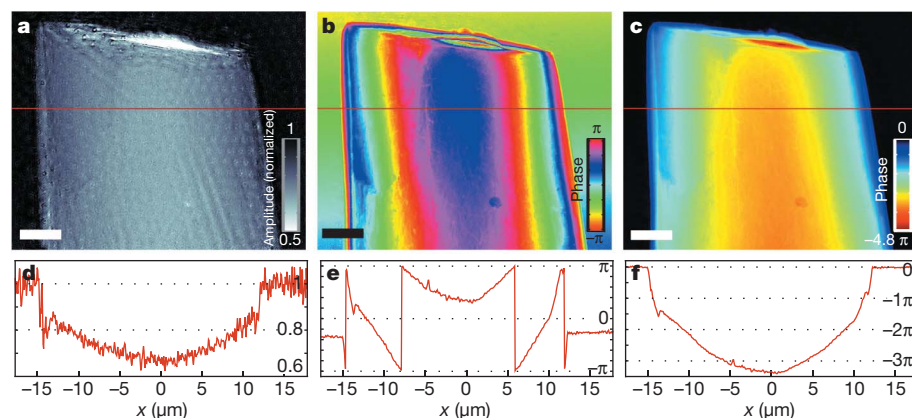
Figure 2 | Projection images reconstructed from ptychographic data. **a**, Reconstructed amplitude of the complex object transmission function normalized with respect to air. Artefacts are visible that are attributed to fluctuations in the X-ray intensity. **b**, Phase part of the complex transmission function. **c**, Phase after linear-ramp correction and unwrapping. **d**, Profile along red line in panel **a**, revealing a low signal-to-noise ratio. **e**, Profile along red line in panel **b**, illustrating the wrapping of the phase into the range $(-\pi, \pi]$. **f**, Profile along red line in panel **c**. Scale bars, 5 μm.
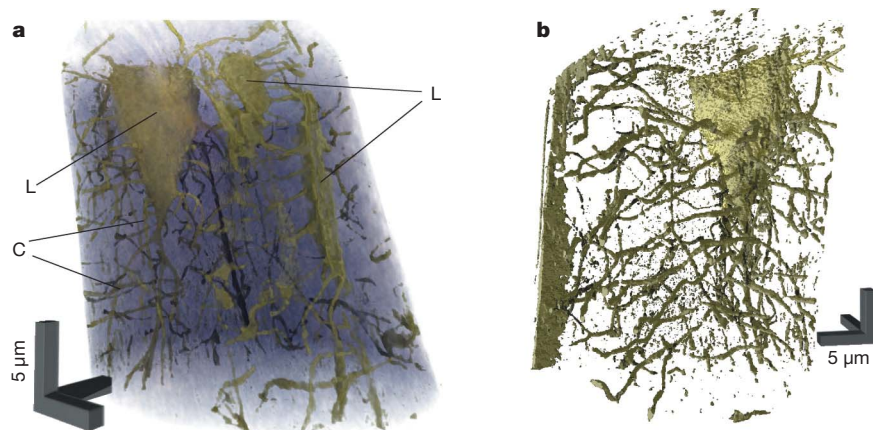
Figure 3 | 3D rendering of the tomographic reconstruction. a,Volume rendering with the bone matrix in translucent colours to show osteocyte lacunae (L) and the connecting canaliculi (C). **b,** Isosurface rendering of the lacuno-canalicular network obtained by segmenting the corresponding peak in the density on histogram shown in Fig. 4c. Morphological analysis of tomographic reconstructions is most often based on this type of segmentation, which is independent of the absolute scale of the density. Long edges of 3D scale bars, 5 μm.

found to fluctuate around 0.62 electrons per Å^3, which can be directly converted to a mass density of 2.0 g cm^{-3}. As expected, this density is slightly higher than the tabulated value[24] of 1.92 g cm^{-3} for human adult cortical bone, which is an average over volumes much larger than our reconstruction voxel, thus including Haversian canals, osteocyte lacunae and other low-density regions. The uncertainty of the density within a reconstruction voxel of about 0.04 electrons per Å^3 is found by computing the standard deviation of the density in the empty space surrounding the sample. This error can be reduced using the statistics of larger regions of interest. For instance, Fig. 4d presents histograms of the voxel values in two $(1\,\mu\text{m})^3$ boxes shown in red and blue in Fig. 4a and b. Whereas the width of these distributions is consistent with the voxel variance, the position of the peaks can be determined with much higher precision. At a 1-μm scale, we find that relative variations of less than 0.2% in electron density can be measured, which corresponds to about 5 mg cm^{-3} in mass density. Such high precision could be invaluable to define or refine absolute standards for the diagnostic of diseases affecting bone tissues.

The most common 3D CDI reconstruction scheme considered up to now was inspired from crystallography and involved carrying out phase retrieval directly in 3D space[25,26]. This approach however is limited to samples that have been completely isolated and to the weak scattering regime (that is, where the first Born approximation is valid).

With a sample placed directly on a holder and no membrane obstructing any range of projection angles, and with X-ray phase shifts up to nearly 4π, our results clearly show that ptychographic X-ray computed tomography has a much wider field of application. The current limitations of our tomography method are technical rather than fundamental. Like most hard X-ray imaging techniques, our method demands little sample preparation. The sample used in this work was made vacuum-compatible only to be imaged also by a scanning electron microscope. For the present results, resolution is mostly flux-limited, that is, it depends on decreasing photon counts at larger scattering angles. Ultimately, resolution is limited by radiation damage, mechanical instabilities and imprecision in the relative positioning of pinhole and sample, which may create weak distortions in the projections and thus have a detrimental effect on the subsequent tomographic reconstruction. With a total of 2×10^{11} incident photons, about 1.1×10^9 per projection, the total radiation dose on the sample is evaluated to be about 2 MGy (11.4 kGy per projection), much less than the feature-destroying limit for a resolution of 150 nm (ref. 27). Data acquisition for this exploratory study was about 40 h. Since then, acquisition times at the same instrument have been reduced by approximately a factor of five and will ultimately be limited by the coherent flux of the source and the dead time of various hardware components. Carrying out the same experiment at
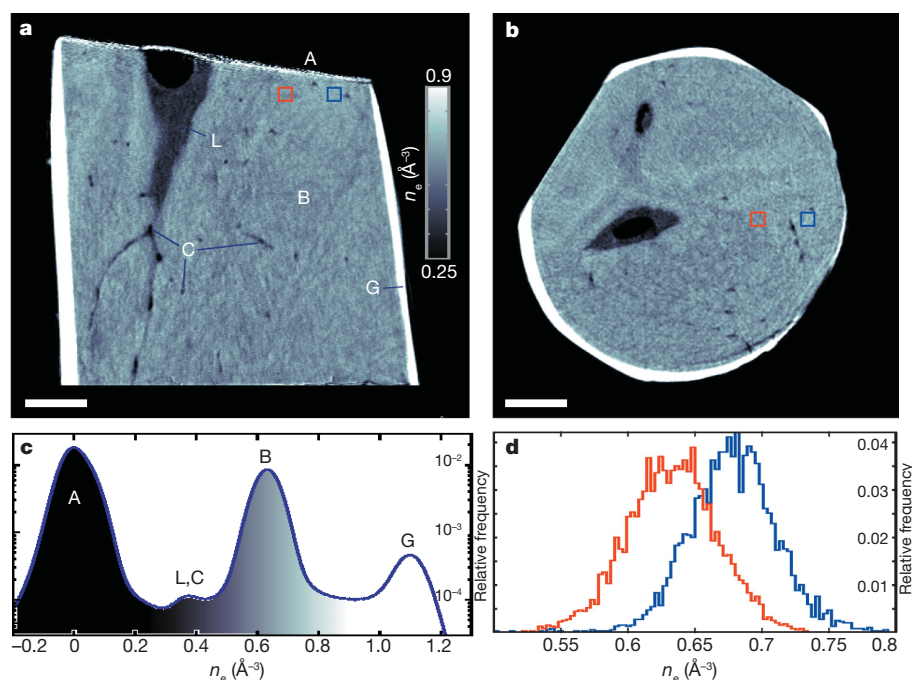
Figure 4 | Result of tomographic phase reconstruction. a, Cut parallel to the rotation axis through the reconstructed volume. The phase values have been converted to quantitative electron density n_e (linear greyscale). The labelled structures are air (A), bone matrix (B), canaliculi (C), gallium coating (G), which is a result of focused ion beam preparation, and osteocyte lacuna (L). **b,** Cut perpendicular to the rotation axis. The two large dark areas are osteocyte lacunae, and small dark dots are sections through individual canaliculi. The slight variations in the shades of grey in **a** and **b** indicate inhomogeneity in the bone density at the submicrometre scale. **c,** Histogram of electron density values in the reconstructed volume (500 equally sized bins for n_e values between -0.2 and 1.3 Å^{-3}). The labels correspond to the ones in panel **a** and indicate the grey values that can be associated with the aforementioned features. **d,** Comparison of the bone peak (label B) of the histogram for two cubic sub-volumes of 1 μm^3, indicated by the red and blue boxes in **a** and **b**. At the micrometre scale, the detection threshold of density fluctuations is slightly less than 0.001 Å^{-3} or about 0.2% of the mean bone density. Scale bars in **a** and **b**, 5 μm.

a brighter source should reduce the measuring time to a few hours or less.

The reconstruction of the density of a mouse femur sample presented here gives a glimpse of the new research avenues such a high-resolution quantitative tomography method can provide. The absolute scale of the reconstructed density will make possible accurate comparisons of multiple samples. A promising application in biomedical research is the imaging of bone biopsies on the nanoscale to study the early development of diseases such as osteoporosis and to evaluate treatment successes in preclinical studies and clinical trials. Materials science applications can also benefit from the combination of high resolution and high electron density contrast, for instance to localize density variations in polycrystalline alloys. Though readily accessible with current sources, the technique will benefit from the high brilliance and coherence of X-rays produced by state-of-the-art and next-generation synchrotron facilities such as PETRA III (Hamburg, Germany), NSLS II (Brookhaven, USA) and the Cornell ERL (Ithaca, USA) where the same type of analysis could be performed at even shorter wavelengths, thus increasing both the penetration depth and the depth of field.

METHODS SUMMARY

Sample preparation. A mouse femur was dissected, cleaned from soft tissue and underwent an ethanol dehydrating series before further processing steps. After resin-embedding the specimens were then machined with a high-speed milling system to access a mid-diaphyseal cross-section. Finally, focused ion beam milling was performed to prepare a roughly cylindrical specimen of about 25 μm in diameter and 35 μm in height.

Experiment. Experiments were carried out at the X12SA (cSAXS) beamline of the Swiss Light Source. A pinhole of around 2.3 μm in diameter was put into a mono-chromatic 6.2 keV X-ray beam to create the small localized illumination required for sufficient sampling of the diffraction patterns with the detector. Diffraction patterns were collected with a PILATUS 2M detector[28]. The scan points were 1.2 μm apart from each other, ensuring sufficient overlap of the illuminated areas in the reconstruction. 181 projections with 704 scan points each were collected at tilt angles between −90 and 90 degrees with one degree angular spacing. The total exposure time was 36 h.

Reconstruction. The projection images (see Fig. 2) were reconstructed using a ptychographic algorithm with simultaneous retrieval of the illumination function[29]. The central 128 × 128 pixels of each diffraction pattern were used, resulting in a pixel size in the reconstruction of about 65 nm × 65 nm. The projections were aligned with respect to each other while the phase was unwrapped with a quality-map (squared gradient) path following the method of ref. 30 in the 2D projection images and further refined iteratively by enforcing self-consistency in the sinograms. The tomographic reconstruction was performed using standard filtered back-projection with Hamming filter and linear interpolation, resulting after a conversion step in a volume representation of the specimen's electron density with isotropic voxels of about 65 nm edge length.

Full Methods and any associated references are available in the online version of the paper at www.nature.com/nature.

1. Yin, G. et al. Energy-tunable transmission x-ray microscope for differential contrast imaging with near 60 nm resolution tomography. Appl. Phys. Lett. **88,** 241115 (2006).
2. Parkinson, D. Y. et al. Quantitative 3-D imaging of eukaryotic cells using soft X-ray tomography. J. Struct. Biol. **162,** 380–386 (2008).
3. Haddad, W. S. et al. Ultrahigh-resolution X-ray tomography. Science **266,** 1213–1215 (1994).
4. Chu, Y. S. et al. Hard-x-ray microscopy with Fresnel zone plates reaches 40 nm Rayleigh resolution. Appl. Phys. Lett. **92,** 103119 (2008).
5. Cloetens, P. et al. Phase objects in synchrotron radiation hard x-ray imaging. J. Phys. D **29,** 133–146 (1996).
6. Wilkins, S. W. et al. Phase-contrast imaging using polychromatic hard X-rays. Nature **384,** 335–338 (1996).
7. Nugent, K. Coherent methods in the X-ray sciences. Adv. Phys. **59,** 1–99 (2010).
8. Rodenburg, J. M. Ptychography and related diffractive imaging methods. Adv. Imaging Electron Phys. **150,** 87–184 (2008).
9. Thibault, P. et al. High-resolution scanning x-ray diffraction microscopy. Science **321,** 379–382 (2008).
10. Davis, T. J. et al. Phase-contrast imaging of weakly absorbing materials using hard X-rays. Nature **373,** 595–598 (1995).
11. Nugent, K. et al. Quantitative phase imaging using hard X rays. Phys. Rev. Lett. **77,** 2961–2964 (1996).
12. Momose, A. et al. Phase-contrast X-ray computed tomography for observing biological soft tissues. Nature Med. **2,** 473–475 (1996).
13. Pfeiffer, F. et al. Phase retrieval and differential phase-contrast imaging with low-brilliance X-ray sources. Nature Phys. **2,** 258–261 (2006).
14. Faulkner, H. M. & Rodenburg, J. M. Movable aperture lensless transmission microscopy: a novel phase retrieval algorithm. Phys. Rev. Lett. **93,** 023903 (2004).
15. Rodenburg, J. et al. Hard-x-ray lensless imaging of extended objects. Phys. Rev. Lett. **98,** 034801 (2007).
16. Guizar-Sicairos, M. & Fienup, J. R. Phase retrieval with transverse translation diversity: a nonlinear optimization approach. Opt. Express **16,** 7264–7278 (2008).
17. Giewekemeyer, K. et al. Quantitative biological imaging by ptychographic x-ray diffraction microscopy. Proc. Natl Acad. Sci. USA **107,** 529–534 (2010).
18. Dierolf, M. et al. Ptychographic coherent diffractive imaging of weakly scattering specimens. N. J. Phys. **12,** 035017 (2010).
19. Schropp, A. et al. Hard x-ray nanobeam characterization by coherent diffraction microscopy. Appl. Phys. Lett. **96,** 091102 (2010).
20. Vine, D. J. et al. Ptychographic Fresnel coherent diffractive imaging. Phys. Rev. A **80,** 063823 (2009).
21. Morrison, G. R. & Chapman, J. N. A comparison of three differential phase contrast systems suitable for use in STEM. Optik **64,** 1–12 (1983).
22. Schneider, P. et al. Towards quantitative 3D imaging of the osteocyte lacuno-canalicular network. Bone. doi:10.1016/j.bone.2010.07.026 (2010).
23. Kamioka, H. et al. A method for observing silver-stained osteocytes in situ in 3-m sections using ultra-high voltage electron microscopy. Microsc. Microanal. **15,** 377–383 (2009).
24. Hubbell, J. & Seltzer, M. Tables of X-ray Mass Attenuation Coefficients and Mass Energy-Absorption Coefficients. Version 1.4, Report NISTIR-5632 (National Institute of Standards and Technology, 1995) ⟨http://physics.nist.gov/xaamdi⟩.
25. Chapman, H. N. et al. High-resolution ab initio three-dimensional x-ray diffraction microscopy. J. Opt. Soc. Am. A **23,** 1179–1200 (2006).
26. Nishino, Y. et al. Three-dimensional visualization of a human chromosome using coherent x-ray diffraction. Phys. Rev. Lett. **102,** 018101 (2009).
27. Howells, M. et al. An assessment of the resolution limitation due to radiation-damage in X-ray diffraction microscopy. J. Electron Spectrosc. Relat. Phenom. **170,** 4–12 (2009).
28. Kraft, P. et al. Performance of single-photon-counting PILATUS detector modules. J. Synchrotron Radiat. **16,** 368–375 (2009).
29. Thibault, P. et al. Probe retrieval in ptychographic coherent diffractive imaging. Ultramicroscopy **109,** 338–343 (2009).
30. Ghiglia, D. C. & Pritt, M. D. Two-Dimensional Phase Unwrapping: Theory, Algorithms And Software (Wiley, 1998).

Author Contributions A.M., R.W., M.D., P.T., O.B., and F.P. conceived the experiment. R.W. prepared the sample. A.M., C.M.K., P.T., M.D., O.B. and F.P. carried out the experiment. P.T., M.D., C.M.K. and P.S. analysed the data. All authors discussed the results and contributed to the final manuscript.

Author Information Reprints and permissions information is available at www.nature.com/reprints. The authors declare no competing financial interests. Readers are welcome to comment on the online version of this article at www.nature.com/nature. Correspondence and requests for materials should be addressed to P.T. (pierre.thibault@tum.de).

METHODS

Sample preparation. Femora of twelve-week-old C57BL/6 (B6) mice were dissected and cleaned from soft tissue. After cutting the femora into halves using a scalpel, bone marrow was washed out using a 70% ethanol steam. Bones were stored in 70% ethanol and underwent an ethanol dehydrating series before further processing steps. Bones were infiltrated at four stages with a progressively increasing ratio of Lowicryl HM20 (from Polyscience, Chemie Brunschwig AG) to ethanol and a progressively decreasing temperature from 0 °C to −50 °C. The resin was subsequently polymerized for more than two days at −50 °C using ultraviolet radiation. The embedded specimens were then machined with a high-speed milling system (Leica EM TRIM2) to access a mid-diaphyseal cross-section. Finally, focused ion beam milling was performed on a CrossBeam workstation (NVision 40; Carl Zeiss SMT) to prepare a roughly cylindrical specimen of about 25 μm in diameter and 35 μm in height.

Experiment. Experiments were carried out at the X12SA (cSAXS) beamline of the Swiss Light Source. A pinhole of around 2.3 μm in diameter milled into a 50-μm-thick tungsten foil by focused ion beam was put into a monochromatic 6.2-keV X-ray beam to create the small localized illumination required for sufficient sampling of the diffraction patterns with the detector. The sample was mounted on a three-axis piezo-driven scanning stage on top of an air-bearing rotation stage. A helium-flushed flight path was inserted between sample and detector to suppress air scattering and absorption. Diffraction patterns were collected with a PILATUS 2M detector[28] placed 7.18 m downstream of the sample. To avoid an ambiguity inherent to ptychographic reconstructions from diffraction data collected with a regular raster scan[29], the scan points were located on concentric circles[18] (see Fig. 1b). The scan points were 1.2 μm apart from each other, ensuring sufficient overlap of the illuminated areas in the reconstruction. At each projection angle, 704 coherent diffraction patterns with 1 s exposure time each were taken. 181 projections were collected at tilt angles between −90 and 90 degrees with one degree angular spacing. The total exposure time was 36 h.

Reconstruction. The high-resolution projection images (see Fig. 2) were reconstructed using a ptychographic algorithm with simultaneous retrieval of the illumination function[29]. The central 128×128 pixels of each diffraction pattern were used, resulting in a pixel size in the reconstruction of about 65 nm × 65 nm. The projections were cropped to 617×499 pixels. They were aligned vertically by detecting the upper edge of the specimen and horizontally by computing the centre of mass of a section of the specimen. The phase was first unwrapped in the 2D projection images with a path-following method using the squared gradient of the phase as a quality map[30]. Remaining errors caused by large phase shifts at the specimen's sharp edges were reduced iteratively by enforcing self-consistency in the sinograms. The tomographic reconstruction was performed using standard filtered back-projection with Hamming filter and linear interpolation, resulting in a volume of $617 \times 617 \times 499$ isotropic voxels with an edge length of about 65 nm. Conversion to electron density was done using the relations $\delta = -\Phi_{\Delta r} \cdot \lambda / (2\pi \Delta r)$ and $n_e = 2\pi / (r_e \cdot \lambda^2 \delta)$ with $\Phi_{\Delta r}$ being the reconstructed phase shift value for a voxel of side length Δr, δ the real part of the object's complex refractive index, λ the X-ray wavelength and r_e the classical electron radius.